

1 Spatial influence of agricultural residue burning and aerosols on land surface
2 temperature

3 Akanksha Pandey¹, Richa Singh¹, Kumari Aditi^{1,2}, Neha Chhillar¹, Tirthankar Banerjee^{1,2*}

4

5 ¹ Institute of Environment and Sustainable Development, Banaras Hindu University, Varanasi, India.

6 ²DST-Mahamana Centre of Excellence in Climate Change Research, Banaras Hindu University, Varanasi, India.

7 *Correspondence to: T. Banerjee (tb.iesd@bhu.ac.in; tirthankaronline@gmail.com)

8

9 Abstract

10 The biophysical effects of agricultural residue burning, driven by the excessive release of
11 energy and carbonaceous aerosols, remain poorly quantified at the global scale. Residue-
12 based fires have the potential to modify regional climate by altering land surface temperature
13 (LST), highlighting the need for investigation at regional scale. Here, an observation-driven
14 assessment of spatial variations in LST due to concurrent release of energy and aerosols has
15 been made over northwestern India using multiple satellite and reanalysis-based datasets.
16 Year-specific fire pixel density was used to delineate an intensive fire zone characterized by
17 medium-to-large residue-based fire. Geospatial analysis revealed positive association among
18 FRP (fire radiative power), LST and AOD (aerosol optical depth). Over intensive fire zone, a
19 space-for-time approach revealed significant increase in both Δ LST (0.57°C; 95% CI:0.33-
20 0.81°C) and Δ AOD (0.13; 95% CI:0.08–0.17) due to fire. Random Forest non-linear model was
21 employed to regress potential influence of FRP and AOD on LST having several other variables
22 as confounding factors. FRP consistently emerged as the dominant predictor of LST, followed
23 by planetary boundary layer height and aerosols. An increase in relative feature importance
24 of FRP was noted during days having high fire intensity and positive association with LST.
25 Geographically weighted regression further explained spatial heterogeneity in LST
26 modulation by FRP. Overall, this analysis provides the first empirical evidence that residue-
27 based fire contributes to changes in land surface temperature. It further highlights that the
28 magnitude of this perturbation is governed by interannual variations in fire intensity and
29 influenced strongly by prevailing meteorological conditions.

30 **Keywords:** Aerosols, Biomass burning, Fire, GWR, Random Forest.

31

32

33

34 **Introduction**

35 Burning agricultural residues is a widespread practice for the rapid removal of post-
36 harvest biomass from croplands in many regions of the world (Streets et al., 2003; Singh et
37 al., 2018; Shyamsundar et al., 2019). While biomass burning is often associated with
38 deforestation (Chuvieco et al., 2021), forest fires (van der Velde et al., 2021; Aditi et al., 2025),
39 and shifting cultivation (Prasad et al., 2000), residue burning on agricultural land is primarily
40 conducted to clear fields, fertilize soil, eradicate weeds and pests, and prepare land for the
41 next crop cycle (Graham et al., 2002; Korontzi et al., 2006; Lan et al., 2022). This practice is
42 observed across large agricultural regions globally, including China (Streets et al., 2003; Zhang
43 et al., 2020), South America (Graham et al., 2002), Southeast Asia (Lasko and Vadrevu, 2018;
44 Yin, 2020), and northwestern India (Singh et al., 2018, 2021; Sarkar et al., 2018). In
45 northwestern India, extensive residue burning during October to November is a recurring
46 phenomenon and has been widely examined from multiple perspectives. Previous studies
47 report that these burning events contribute to severe air-quality degradation in downwind
48 urban centers (Singh et al., 2018; Jethva et al., 2019), alter aerosol loading and chemistry
49 (Mhawish et al., 2022), modify aerosol vertical stratification and radiative forcing (Hsu et al.,
50 2003; Vinjamuri et al., 2020; Banerjee et al., 2021), induce adverse health effects (Singh et al.,
51 2021), and may influence regional hydrological processes (Kant et al., 2023). However, limited
52 attention has been paid to investigate its effect on urban climate, especially on modulating
53 lower atmospheric thermal budget which has been otherwise strongly evident in case of
54 forest fire (Liu et al., 2018, 2019).

55 Across the northwestern India, dual cropping pattern including rice and wheat crop is
56 predominately practised over roughly 4.1 million ha of land (NAAS, 2017). Such a cropping
57 pattern leads to generation of huge crop residues that are low in nutrient content and rich in
58 silica and ash. Typically, residues from rice-wheat cropping system possess limited economic
59 value, as they are unsuitable for use as alternative fodder, bioenergy feedstock or as raw
60 material in pulp and paper industry (Shyamsundar et al., 2019; Lan et al., 2022). Besides, with
61 the introduction of mechanical harvester in the 1980s and enactment of groundwater
62 preservation act in the late 2000s, in situ burning of agricultural residues has become a
63 recurrent practice among the local farmers. This practice serves to expedite field clearance
64 and reduce the turnaround period between rice harvest and the subsequent sowing of the

65 wheat crop (Balwinder-Singh et al., 2019). India produces an estimated 500 million metric
66 tonnes (MT) of crop residues annually, of which 20–25% are disposed of through open-field
67 burning. Crop residue burning is particularly prevalent in northwestern India, where roughly
68 20-25 MT of residues are set on fire each year (Balwinder-Singh et al., 2019; Lan et al., 2022).
69 Unregulated residue burning in this region contributes approximately 300 Gg/yr of PM_{2.5} and
70 50 Tg of CO₂ equivalent green-house gas emission (Singh et al., 2020). Notably, the frequency
71 of fire incidences has exhibited a persistent upward trend, coinciding with concurrent
72 increases in vegetation indices and atmospheric aerosol loading (Vadrevu et al., 2019; Jethva
73 et al., 2019). In addition to atmospheric emissions, fires exert numerous biophysical impacts
74 on the surrounding ecosystems. Fire induces a cascade of consequential processes, including
75 modifications to the surface energy balance, redistribution of nutrients, alterations in species
76 composition, changes in surface albedo, and variations in evapotranspiration rate (Ward et
77 al., 2012; Liu et al., 2019). Additionally, fire can induce certain biogeochemical and biophysical
78 stresses on local environment by modifying atmospheric composition and surface properties
79 (Andela et al., 2017; Aditi et al., 2025). Such transformation of the native landscape, coupled
80 with excessive release of energy, aerosols and its precursors, may therefore have several
81 potential implications on the environment.

82 Most studies on biomass-based fires have focused on identifying land–atmosphere
83 processes responsible for fire initiation and propagation, quantifying emissions, and
84 evaluating fire-induced land–atmosphere exchanges (Lasko and Vadrevu, 2018; Jethva et al.,
85 2019; Chuvieco et al., 2021; Aditi et al., 2025). In contrast, there is a paucity of knowledge
86 regarding how biomass burning contributes to climate feedbacks through modifications of
87 Earth’s surface radiative budget and land surface temperature (Bowman et al., 2009; Andela
88 et al., 2017). Plausible explanation to this includes limited observation and associated
89 uncertainties in estimating key biophysical parameter like surface albedo, land-atmosphere
90 exchange of sensible heat flux and water vapor, changes in evapotranspiration before and
91 after fire events. There are instances when global forest fire incidences and size have been
92 linked with modifications in land surface temperature (LST; Alkama and Cescatti, 2016; Liu et
93 al., 2018, 2019). Likewise, Liu et al. (2019) noted an enhancement in mean annual LST over
94 burned forest area in the northern high latitudes. Similar evidence of increase in summertime
95 surface radiometric temperature over temperate and boreal forests in the Northern

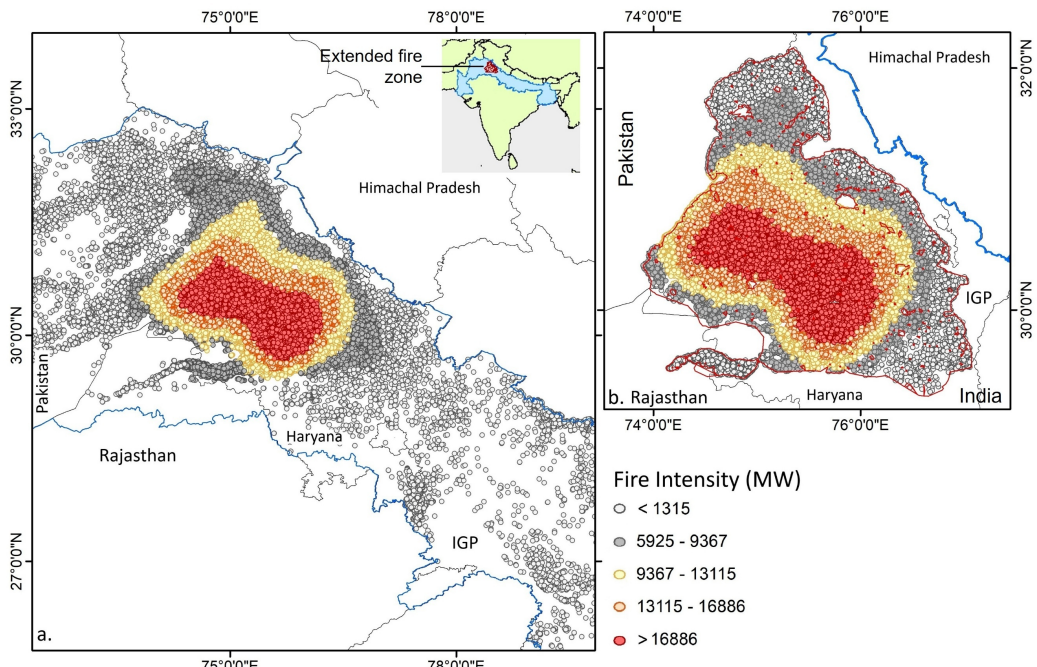
96 Hemisphere was accounted by Zhao *et al.* (2024). Alkama and Cescatti (2016) reported
97 increases in mean and maximum air temperature over arid regions following forest loss,
98 highlighting the sensitivity of surface temperature to land-cover modification. However, fire-
99 induced thermal forcing is strongly constrained by the fire size (Zhao *et al.*, 2024). Small, short-
100 lived fires, such as those associated with agricultural residue burning, often fail to produce
101 sufficiently large changes in surface albedo or evapotranspiration, and therefore may not
102 generate a detectable LST response. Incidence of elevated LST over different provinces in
103 China due to agricultural residue burning has only recently reported by Zhang *et al.* (2020). A
104 spatially heterogeneous increase in LST correlated strongly with fire count, with highest LST
105 gradient noted at distances of 4–10 km from the central point of crop residue burning and
106 persisting for 1–3 days. In contrast, the effects of post-harvest fire incidences in northwestern
107 India on LST remain largely unexplored. This gap introduces considerable uncertainty in
108 assessing the climate feedback of crop residue burning and highlights the need for a better
109 understanding of the underlying mechanisms.

110 This study aims to explore immediate biophysical effect of agricultural residue fire on
111 surface temperature over northwestern India. By integrating spatially and temporally
112 consistent satellite observations and reanalysis datasets, including fire counts, fire radiative
113 power, land surface temperature, aerosols, meteorological covariates, topography, surface
114 property, and physical environment over intensive fire zone, we sought to quantify time-
115 bound changes in LST in response to variations in fire intensity and aerosol loading. Several
116 statistical methods were applied to construct the changes in LST with fire severity and
117 aerosols. Additionally, a space-for-time framework was followed to assess the effects of
118 recurrent FRP variations on LST and aerosol optical depth (AOD) throughout the fire season.
119 Specifically, we addressed two key questions: (1) Does LST respond to changes in fire intensity
120 over northwestern India? and (2) How do local meteorology and aerosol loading modulate
121 LST variation with respect to space and time? To the best of our knowledge, this is the first
122 systematic assessment of agricultural residue fire–driven modulations in LST over
123 northwestern India. By integrating multiple geospatial observations, the analysis offers critical
124 insights into the biophysical feedbacks of residue-based fire and advances understanding of
125 LST responses to residue burning. Further, it refines estimates of fire-induced perturbations

126 in the regional radiative budget offering valuable representation of biomass-based fire in
127 Earth system models.

128 **2. Dataset and methodology**

129 **2.1 Study domain**



130
131 Fig. 1. Spatial variation in satellite-based fire radiative power across northwest India,
132 distribution of FRP-based fire intensity (MW/pixel) (a) and domain selected for
133 retrieval and processing of SNPP VIIRS FRP, AOD and Aqua MODIS LST (b). The region
134 marked with blue in Fig. 1a subset indicates the Indo-Gangetic Plain (IGP) spanning
135 from Pakistan to Bangladesh through India. The extended fire zone selected for
136 analysis is marked with red within the IGP and has been shown in detail in Fig. 1a with
137 fire pixel density. *Disclaimer note:* The international boundaries shown on this map are
138 for illustrative purposes based on the 'Survey of India' archive. They do not imply
139 endorsement of acceptance by the journal or publisher of any particular political or
140 legal status of the territories depicted.

141
142 Post-harvest biomass burning is predominantly practiced across the northwestern
143 Indo-Gangetic Plain (IGP) of South Asia, particularly in the agrarian states of Punjab and
144 Haryana, which together contribute nearly 60–70% of India's total food grain production. The
145 concurrent rise in rice and wheat cultivation has led to a substantial increase in crop residue

146 generation, resulting in higher fire intensity in recent years (Jethva et al., 2019). In this study,
147 geospatial analyses of LST, fire activity, and aerosol loading were conducted over
148 northwestern India during October–November between 2017 and 2021. The combination of
149 high agricultural output, extensive biomass burning, and increasing fire activity makes this
150 region particularly suitable for investigating fire dynamics and their environmental
151 implications. Schematic workflow indicating core datasets and adopted methodology for
152 exploring FRP-AOD-LST association is illustrated in Fig. S1. Instead of defining a fixed spatial
153 domain a priori, year-wise fire signals were retrieved across cropland areas in northwestern
154 India. This approach allowed the delineation of a core study region that varied annually
155 according to year-specific fire intensity and spatial trends (as shown in Fig. S2), but all
156 eventually bound to 29.2770° to 32.1625° N and 73.8996° to 77.0718° E, as illustrated in Fig.
157 1b.

158 **2.2 Spatial dataset**

159 Active fire count data was retrieved from the standard fire product of Visible Infrared
160 Imaging Radiometer Suite (VIIRS) Collection-2 (VNP14IMG) available at 6-min L2 swath at 375
161 m resolution. The VIIRS onboard the Suomi National Polar-orbiting Partnership (SNPP) satellite
162 is a cross-track single-angle scanning radiometer which was launched in year 2011 under joint
163 operation of NASA and NOAA. The VIIRS fire detection algorithm typically extends well refined
164 and validated MODIS Fire and Thermal Anomalies product (Giglio et al., 2003). The I-band
165 based fire detection algorithm primarily utilizes brightness temperature of Channel I4 on
166 middle infrared spanning from 3.55 to 3.93 μm , centred at 3.74 μm . Additionally, to isolate
167 the active fire spots from the fire-free background channel, a single gain I5 at thermal infrared
168 regions (10.5–12.4 μm) is also considered. Rest of the I-band channels i.e. I1 to I3, covering
169 visible, near and short-wave IR are used to distinguish pixels with cloud, water and sun-glint
170 (Schroeder et al., 2014). The VIIRS fire database was considered due to its superior precision
171 and accuracy in identifying relatively small fire, greater spatial resolution at footprint and pixel
172 saturation temperature (Li et al., 2018; Vadrevu and Lasko, 2018; Aditi et al., 2023). For this
173 experiment, SNPP VIIRS 375 m L2 active fire count data with nominal (fire mask class 8) and
174 high confidence (fire mask class 9), was retrieved over northwestern India from year 2017 to
175 2021 (all inclusive).

176 Fire radiative power (FRP) quantifies the release of radiative energy from biomass
177 burning integrated at all angles and wavelengths over a spatial scale. Measured in Watt, FRP
178 retrieval quantifies the release of heat energy against time and in many instances linearly
179 associated with the rate of fuel consumption and emission (Ichoku et al., 2008; Nguyen and
180 Wooster, 2020). A detailed description on FRP retrieval and comparison among the sensors
181 are available in Wooster et al. (2003, 2005) and Ichoku et al. (2008). Li et al. (2018) concluded
182 VIIRS FRP as comparable with MODIS FRP in most of fire clusters and stable across swath.
183 Here, FRP (MW) was processed from the SNPP VIIRS C2 Level-2 (L2) 375 m active fire product
184 (VNP14IMG). VIIRS FRP was used as a proxy of fire intensity and potential emission strength
185 from the biomass burning area, and considered as a direct measurement of radiative energy
186 being released from individual fire pixel.

187 Land surface temperature (LST, in °C) at 1 km spatial resolution was utilized from
188 Moderate Resolution Imaging Spectroradiometer (MODIS) version 6.1 Land Surface
189 Temperature and Emissivity retrievals product (MYD11A1). Typically, LST indicates
190 thermodynamic temperature of the interface atmospheric layer within soil, plant cover and
191 lower atmosphere, and serves as an indicator of land-atmosphere interaction and exchange
192 (Li et al., 2023). Here, MODIS MYD11A1 radiometric dataset with quality flag '00' was
193 specifically chosen considering its broad swath and wider applicability in estimating land
194 surface temperature. MODIS LST is validated against ground observations on diverse land
195 covers and reported to provide realistic estimate of surface temperature (Wan, 2014) with an
196 uncertainty of ≤ 0.5 K. The dataset includes daytime maximum LST (at 1:30 PM local time) and
197 nighttime minimum LST (at 1:30 AM local time). Here, daytime LST dataset were obtained
198 solely from the MODIS sensor onboard the Aqua satellite to closely coincide with VIIRS fire
199 count observations at 1:30 PM local time, a period when crop residue-based fires are
200 expected to reach at peak.

201 Aerosol optical depth (AOD) from Visible Infrared Imaging Radiometer Suite (VIIRS)
202 sensor on-board SNPP satellite offers accurate estimation of columnar aerosol loading at 550
203 nm over land. Accuracy of VIIRS V1 DB AOD was evaluated extensively over South Asia by Aditi
204 et al. (2023) and reported to provide stable AOD retrieval against AERONET. Sayer et al. (2019)
205 reported an estimated error of $\pm(0.05+20\%)$ in VIIRS Version 1 DB AOD dataset. Here, Deep
206 Blue (DB) Version 1 AOD dataset (AERDB_L2_VIIRS_SNPP Level-2) was used to retrieve AOD

207 with a nominal spatial resolution of 6 km at nadir. Only quality assured AOD (QA \geq 2) was
208 retrieved for the months of October to November over selected spatial domain.

209 Terra/Aqua MODIS land cover data was used to discriminate crop land against the rest
210 to filter out thermal anomalies exclusively over the agriculture land. To achieve this, MODIS
211 L3 V6.1 Global Land Cover type product (MCD12Q1) was retrieved from LAADS DAAC site for
212 year 2017, available at 0.5 km spatial resolution. MODIS land cover types adopts International
213 Geosphere-Biosphere Programme (IGBP) and other land type classification schemes to
214 classify land cover. Here, land cover type 12 (cropland) was earmarked to isolate the
215 agriculture land from its surrounding (Fig. S3).

216 Daily composite data on surface and root-zone soil moisture (SM, $\text{m}^3 \text{m}^{-3}$) available at
217 9 km resolution was obtained from NASA's Soil Moisture Active Passive (SMAP) satellite
218 mission having L-band radar. The Normalized Difference Vegetation Index (NDVI) at 6 km
219 resolution was derived from the VIIRS/SNPP Deep Blue (AERDB_L2_TOA_NDVI) dataset and
220 was utilized to quantify surface vegetation greenness dynamics. Elevation data at 30 m
221 resolution was retrieved from Copernicus DEM - Global and European Digital Elevation Model
222 dataset for year 2015. Surface albedo data was acquired from MCD43 suite of NASA standard
223 product which integrates both Terra and Aqua retrievals. Here, white-sky version 6.1
224 shortwave albedo data (MCD43A3, Albedo_WSA_shortwave) at 500 m pixel resolution with
225 daily-time step (quality score: 0) was used.

226 Lower surface meteorological data including air temperature (AT), total solar radiation
227 flux (SR), precipitation (PR), relative humidity (RH) was procured from European Centre for
228 Medium-Range Weather Forecasts (ECMWF) AgERA5 dataset. The AgERA5 dataset has been
229 generated by Copernicus Climate Change Service (2020) from hourly ECMWF ERA5 dataset for
230 specific agro-ecological based applications. The meteorological data were pre-customized
231 with temporal aggregation aligned to local time zones and spatial enhancement to a 0.1°
232 resolution using grid-based variable-specific regression model. Here, air temperature at 2
233 meters above the surface, total solar radiation flux received at the surface over a 24-hour time
234 period, and relative humidity at 2 m height was selectively used over pre-identified intensive
235 crop-based fire zone. Planetary boundary layer height (PBLH) data at $0.25^\circ \times 0.25^\circ$ resolution
236 was acquired from ECMWF ERA5 for 13:00-14:00 h local time corresponding with VIIRS

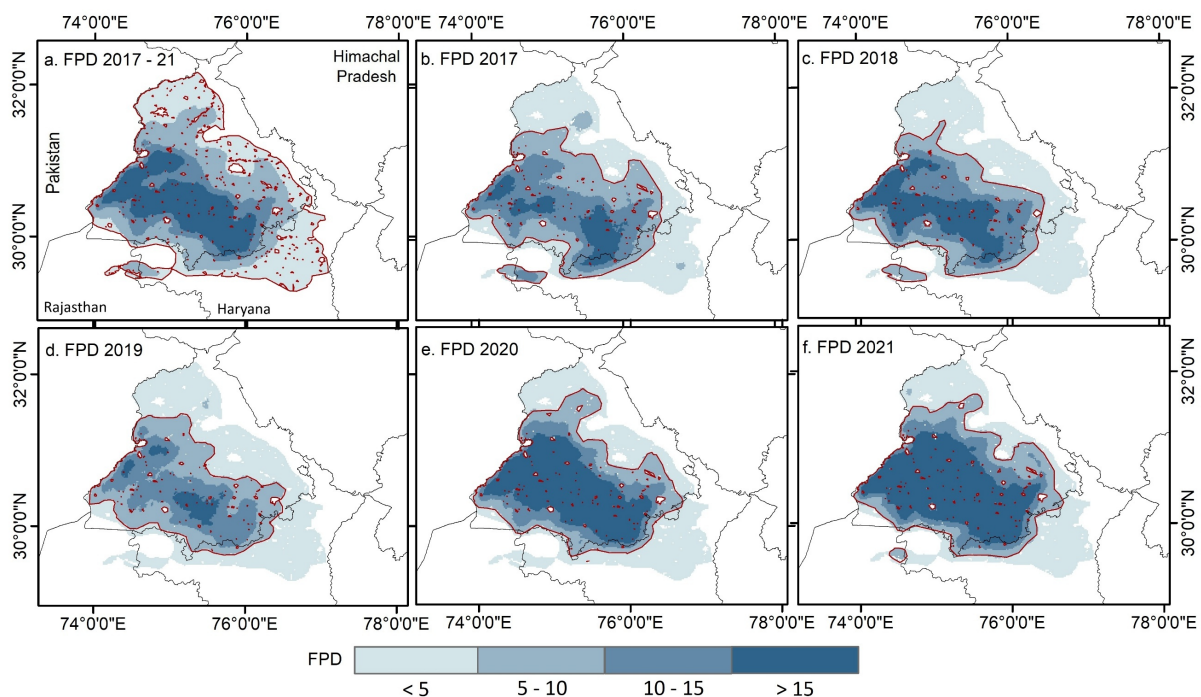
237 overpass time. A description of all core datasets used in this analysis and their resolution,
238 version, and quality flags is included in Table S1 (in supplementary file).

239

240 2.3 Spatial analysis for fire-aerosols-LST association

241 2.3.1 Selection of intensive fire zone

242 Post-harvest residue burning typically begins in mid-October and reaches peak
243 intensity by mid-November across northwestern India. Accordingly, all spatial analyses were
244 conducted for October and November for the years 2017–2021. The VIIRS 375 m fire product
245 successfully retrieved active fire pixels across the Indo-Gangetic Plain, capturing substantial
246 spatial heterogeneity. To ascertain a representative region having predominance of residue-
247 based fire, spatial comparison of fire pixel density was made using daily retrieved VIIRS FRP
248 dataset. FRP was selected instead of fire counts because it directly quantifies the radiative
249 energy released from active burning and therefore provides a more meaningful metric for
250 assessing potential impact on LST. FRP density was computed on a $1.5 \times 1.5 \text{ km}^2$ grid to
251 characterize spatial variations in fire intensity across northwestern India. Following Giglio et
252 al. (2006), FRP density was estimated as the ratio of total FRP within a grid cell to the grid
253 area.



255 Fig. 2. Selection of high intensity residue-based fire zone based on fire radiative power pixel
256 density ($\text{MW } 2.25 \text{ km}^{-2} \text{ day}^{-1}$). Fig. 2a indicates the '*extended geographical region*'

257 demarcating the entire area with varying fire intensity selected for spatial analysis. Rest
258 of the figures classify year-specific '*intensive fire zone*' based on FRP density.
259

260 Initially, geospatial variations in fire intensity and the associated changes in LST and
261 AOD were evaluated. Spatial intercomparison between FRP, LST, and AOD was performed
262 over the region delineated in Fig. 2a. This area was selected to encompass an extended
263 geographical domain without imposing thresholds on low or high FRP density across
264 northwestern India. The region is hereafter referred to as the "extended geographical
265 region," as it integrates fire activity across all years and was used exclusively to establish the
266 spatial association between the predictor (FRP) and dependent variables (LST and AOD).

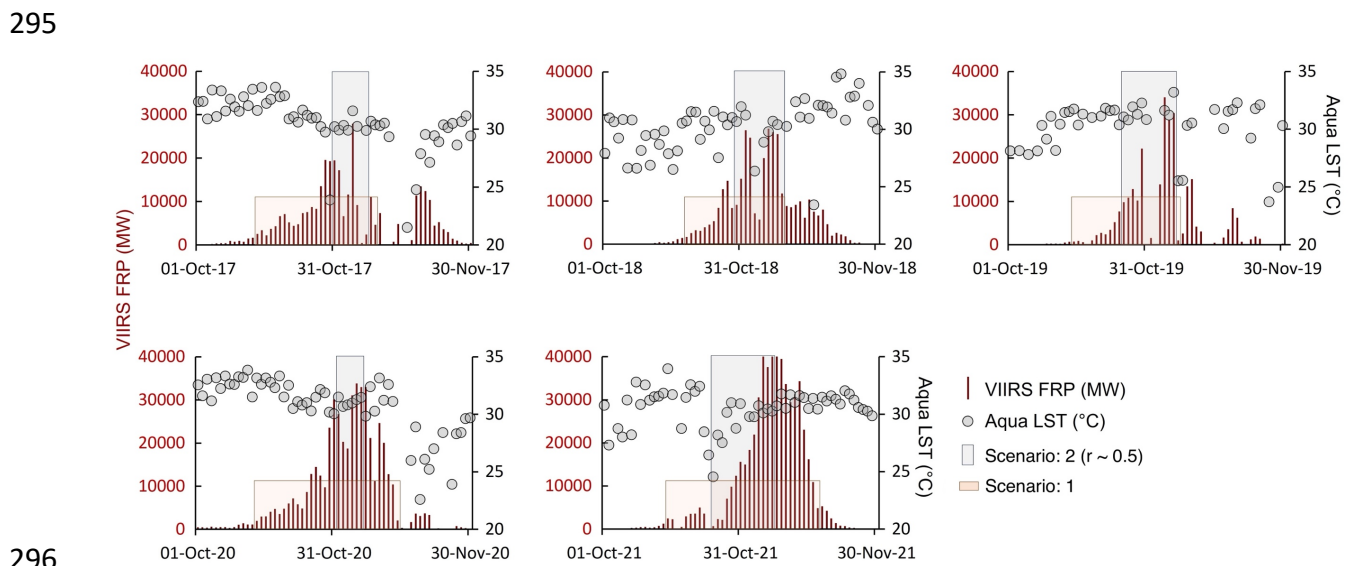
267 In contrast, to assess the day-to-day influence of fire intensity and aerosol loading on
268 LST, a comparatively high-intensity fire zone was delineated relative to low-intensity areas.
269 To achieve this, the entire crop-residue burning region of northwestern India was mapped
270 using a constraint from low FRP density ($<5 \text{ MW grid}^{-1}$) to high FRP density ($>15 \text{ MW grid}^{-1}$).
271 Spatial variations in FRP density were evaluated for each year, and regions with FRP density
272 $>5 \text{ MW grid}^{-1}$ were identified as the "intensive fire zone" (Fig. 2b–f). This threshold ensured a
273 better representation of the effect of medium to large crop-based fire on regional LST as
274 small-intensity fire deem to extinguish faster while being inconducive to considerably
275 influence surface temperature (Zhao et al., 2024).

276 All subsequent spatial datasets used for evaluating FRP–AOD–LST relationships were
277 retrieved exclusively within the year-specific 'intensive fire zone' having FRP density $>5 \text{ MW}$
278 grid^{-1} . Notably, the spatial extent of the high-FRP region remained largely consistent across all
279 years (Fig. 2b–f), with areal estimates summarized in Table S2. It is noteworthy, the region was
280 pre-filtered based on the Terra/Aqua MODIS land cover data to deselect any FRP pixel that
281 emerged from a non-agricultural/crop land.

282 **2.3.2 Selection of temporal window**

283 After isolating the region with higher fire pixel density, the next step was to identify
284 the temporal window in which potential associations between fire intensity and other
285 explanatory variables could be examined. The temporal selection was based on two scenarios,
286 as illustrated in Fig. 3. Scenario 1 was designed to quantify the influence of FRP, aerosols, and
287 other parameters on LST during the period when fire activity begins to intensify and remains

288 persistent over the intensive fire zone. Scenario 1 defines the initiation day as the first instance
 289 in October when aggregate FRP consistently exceeds 1500 MW and shows at least a 50%
 290 increase compared to the previous day. The scenario concludes in November when aggregate
 291 FRP decreases by at least 50% relative to the previous day. The selected dates for Scenario 1
 292 are listed in Table S3, with two exceptions. First, in year 2018 when a >50% criteria was not
 293 met despite having an aggregate FRP >1500 MW and second, in year 2017 when a prior
 294 decrease (>50%) in FRP was avoided because of subsequent rise in fire intensity.



297 Fig. 3. FRP and LST time series over intensive fire zone showing the extent of scenarios used
 298 for geospatial modelling.

299 To define Scenario 2, a statistical association was examined between day-specific
 300 aggregate FRP and the spatially averaged LST. Pixel-based LST values were averaged over the
 301 intensive fire zone and compared against the area-weighted sum of FRP on a day-to-day basis.
 302 A temporal window ("Scenario 2" in Fig. 3) was selected using two criteria: (i) the end of the
 303 window had to coincide with a period of persistently high FRP, and (ii) the window had to
 304 exhibit a strong positive correlation ($r \geq 0.5$) between FRP and regional LST. Such restricted
 305 criteria were put to ensure that we only select year-specific window(s) when FRP (so the fire
 306 count) increases with time and exhibit a strong association with regional LST. Descriptive
 307 statistics of both scenarios are included in Table S4. It is noteworthy that selecting multiple
 308 windows within a year having coinciding days was avoided while ensuring windows should not
 309 contain more than 5% of missing days, irrespective of parameters.

310

311 **2.4 Spatial correlation between fire, aerosols and LST**

312 To examine the spatial association among FRP, LST, and AOD over the residue-based
313 fire zone, grid-based spatial correlation coefficients were computed, and their statistical
314 significance ($p < 0.05$) was tested across the study domain. Daily FRP (375 m) and LST (1 km)
315 datasets were initially resampled to a $6 \times 6 \text{ km}^2$ resolution to match the VIIRS AOD dataset
316 before subject to spatial correlation analyses among the predictor and dependent variables.
317 This approach facilitated the identification of regions exhibiting strong co-variability in thermal
318 conditions corresponding to variations in fire intensity and columnar aerosol loading.

319 **2.5 Hurst Exponent**

320 The Hurst exponent is a statistical measure used to characterize the properties of a
321 time series without imposing assumptions about its underlying distribution. Originally
322 introduced by Hurst (1951) in hydrological studies and later refined by Markonis and
323 Koutsoyiannis (2016), it has since been widely applied across diverse scientific disciplines to
324 analyse long-term trends and variability. In this study, the Hurst exponent was computed for
325 FRP, AOD, and LST time series to identify long-term statistical persistence in the datasets. To
326 estimate the Hurst exponent at the spatial scale, $6 \times 6 \text{ km}^2$ resampled datasets of FRP, AOD,
327 and LST were used. Adjustment of seasonal cycle was not accounted, as the datasets were
328 retrieved and processed exclusively for a single season across the selected years. The main
329 calculation procedures were as follows (Granero et al., 2008):

330 A time series $x(t)$ is given,

$$331 (x)_t = 1/\tau \sum_{t=1}^{\tau} x(t) \quad t = 1, 2, 3 \dots \quad (1)$$

332 The cumulative deviation is determined using Eq. 2:

$$333 X(t, \tau) = \sum_{u=1}^{\tau} (x(u) - (x)_t), \text{ with a condition of } 1 \leq t \leq \tau. \quad (2)$$

334 Extreme deviation sequence, is defined as:

$$335 R(\tau) = \max_{1 \leq t \leq \tau} X(t, \tau) - \min_{1 \leq t \leq \tau} X(t, \tau) \text{ where } \tau = 1, 2, 3 \dots \quad (3)$$

336 The standard deviation sequence is calculated by Eq. (4):

$$337 S(\tau) = [1/\tau \sum_{t=1}^{\tau} (x(t) - (X)_{\tau})^2]^{1/2} \text{ where } \tau = 1, 2, 3 \dots \quad (4)$$

338 By considering both extreme deviation sequence and standard deviation sequence,

339 $R/S = R(\tau)/S(\tau)$ when assuming $(R/S) \propto (\tau/2)^H$ (5)

340 The Hurst exponent ranges between 0 and 1. A value of 0.5 indicates that the time
341 series behaves as a purely stochastic process without persistence, implying that future
342 variations are independent of past behaviour. Values greater than 0.5 denote statistical
343 persistence, reflecting a tendency for future changes to follow the same trend as in the past,
344 with higher values corresponding to stronger persistence. Conversely, values below 0.5
345 indicate anti-persistence, suggesting a tendency for the time series to reverse its trend over
346 time; lower values represent stronger anti-persistence (Peng et al., 2011).

347 **2.6 Space-for-time approach**

348 A space-for-time approach was employed to assess and compare the changes in LST
349 and AOD with respect to FRP within the extended geographical region experiencing recurrent
350 medium- to high-intensity fire. To ensure that changes in LST and AOD were attributable solely
351 to fire activity, grids with similar characteristics in terms of topography, climate, and physical
352 environment were compared (Liu et al., 2019). To achieve this, daily datasets including
353 meteorological covariates (PBLH, AT, SR, RH and PR), physical environment (elevation),
354 vegetation and soil characteristics (NDVI, soil moisture), climatological mean LST and AOD,
355 and surface property (albedo) were extracted over both fire and no-fire grids at a spatial
356 resolution of $10 \times 10 \text{ km}^2$. The daily data were retrieved for each grid under Scenario 2, when
357 FRP reached its peak and exhibited a positive association with regional LST.

358 After filtering out the grid cells with missing LST or AOD values, remaining grids were
359 classified into two groups: those with zero FRP (no-fire) against the grids having $\text{FRP} > 0$,
360 indicating presence of fire. Fire and no-fire grids with comparable spatial characteristics were
361 grouped into a single stratum, and a stratified matching technique was applied to generate
362 multiple strata based on combinations of the selected confounders. Grids were retained only
363 when differences in their physical environment, vegetation and soil characteristics, climate
364 and land cover between fire and no-fire conditions were smaller than the defined thresholds
365 ($\Delta\text{elevation} < 50 \text{ m}$; $\Delta\text{NDVI} < 0.05$; $\Delta\text{soil moisture} < 0.05$; $\Delta\text{albedo} < 0.05$; $\Delta\text{LST} < 10.0$; $\Delta\text{AOD} < 0.80$). Comparisons were then made within strata containing grids of similar attributes to
367 ensure that the observed variations in LST and AOD could be attributed solely to fire activity.
368 The difference in LST (ΔLST) among the fire grids (LST_{fire}) and grids exhibiting no-fire ($\text{LST}_{\text{no-fire}}$)

369 having similar attributes were compared to constitute effect of residue-based fire on LST. A
370 positive (negative) ΔLST ($\text{LST}_{\text{fire}} - \text{LST}_{\text{no-fire}}$) indicates fire-induced warming (cooling) and was
371 used to quantify changes in LST associated with residue burning for the selected years. A
372 similar approach was also adopted to evaluate ΔAOD variations using grid-based retrievals.

373 It is noteworthy that the grids were not classified based on meteorological covariates,
374 as only insignificant variations were noted among the grids. The entire northwestern cropland
375 experiences a relatively uniform background climate during October–November, including
376 comparable boundary layer heights, with PBLH standard deviations ranging from ± 10 m to
377 ± 33 m within a single fire season. The climatological mean LST and AOD were computed only
378 for the pre-fire season (September, 2017–2021), during which none of the grids experienced
379 residue-burning activity. Furthermore, grids were not differentiated by slope or aspect, given
380 the minimal topographic variation across the Gangetic Plain.

381 **2.7 Multicollinearity assessment**

382 Multicollinearity, where independent variables are highly correlated, can distort
383 regression estimates and obscure the true contribution of individual predictors (Graham,
384 2003). To assess this, the Variance Inflation Factor (VIF) for all covariates was calculated using
385 the *statsmodels* library. A VIF of 1 indicates no correlation, values between 1 and 5 suggest
386 moderate correlation, and values greater than 5 are generally interpreted as evidence of
387 substantial multicollinearity (Daoud, 2017). All biophysical, land-surface, and meteorological
388 variables met acceptable VIF thresholds, except solar radiation, which was therefore excluded
389 from Random Forest and GWR analysis. Additionally, soil moisture data was removed from
390 further analysis due to a high percentage of missing observations (~30%).

391 **2.8 Random Forest regression**

392 Random Forest regression was used to model the relationship between the
393 dependent variable (LST) and predictor variables (AOD, PBLH, AT, RH, SR, PR, NDVI, elevation,
394 albedo, and FRP) within the intensive fire zone. Daily retrievals, averaged over the year-
395 specific intensive fire area, were incorporated into the ensemble framework to capture
396 potential non-linear associations among variables. The selected approach ensures robustness
397 to multicollinearity, minimizes overfitting, and effectively captures complex predictor
398 interactions.

399 Random Forest is a non-linear ensemble machine learning algorithm that constructs
400 multiple decision trees from bootstrapped samples of the training data, with a random subset
401 of predictors evaluated at each split. Final predictions are obtained by averaging all trees,
402 improving generalization and reducing overfitting (Breiman, 2001; Puissant et al., 2014). The
403 algorithm was selected due to its strong predictive capability, scalability to large
404 environmental datasets, resilience to correlated inputs, and demonstrated success in
405 previous LST-related studies (Logan et al., 2020; Wang et al., 2022; Zhang et al., 2025). These
406 attributes collectively support Random Forest as an appropriate and interpretable choice for
407 assessing the complex interactions between fire intensity, aerosol loading, and LST dynamics.

408 Key Random Forest hyperparameters (n_estimators, max_depth, min_samples_split,
409 min_samples_leaf, and max_features) were optimized using Bayesian optimization
410 implemented via BayesSearchCV in *scikit-optimize* (Snoek et al., 2012; Shahriari et al., 2015;
411 Frazier, 2018). This adaptive, probabilistic search strategy efficiently identifies near-optimal
412 hyperparameter combinations while minimizing computational cost. To ensure robust model
413 evaluation and mitigate temporal dependence, we employed temporal block cross-validation
414 using a 3-fold GroupKFold in the *scikit-learn* library, where all observations from a given year
415 were assigned to the same fold. This approach prevented temporal overlap between training
416 and validation datasets and reduced information leakage across years. This approach also
417 minimized temporal autocorrelation and prevented data leakage across time periods. Model
418 performance was quantified using cross-validated coefficient of determination (R^2), Root
419 Mean Squared Error (RMSE), and Mean Absolute Error (MAE), providing a comprehensive
420 assessment of model accuracy and prediction error.

421 **2.9 Assessment of relative feature importance**

422 Variable importance was derived from the trained RF model using the mean decrease
423 in impurity method, which quantifies each predictor's relative contribution to reducing
424 variance in model predictions. This approach provides insight into the dominant factors
425 governing the spatial and temporal variability of LST. Feature importance values were
426 extracted and ranked to identify the most influential predictors under different fire intensity
427 scenarios. To enable direct comparison among predictors, the relative contribution of each
428 feature was expressed as its importance score normalized by the sum of all feature
429 importances. As Scikit-learn's `RandomForestRegressor.feature_importances_` inherently

430 returns normalized values summing to one, the reported scores directly represent each
431 predictor's proportional influence within the model.

432 **2.10 Spatial heterogeneity assessment using GWR**

433 Spatial heterogeneity in the influence of FRP, AOD, and other spatial predictors on LST
434 within the intensive fire zone was assessed using Geographically weighted regression (GWR)
435 at 1x1 km² grid. GWR is a spatially explicit regression technique designed to quantify how
436 relationships between predictors and a dependent variable vary across geographic space by
437 estimating spatially varying coefficients (Brunsdon et al., 1996). The method applies a
438 distance-based weighting scheme, whereby observations closer to a given location receive
439 higher weights, allowing local parameter estimation that reflects neighbourhood-specific
440 dynamics (Yang et al., 2020). Unlike global regression models that assume spatial stationarity,
441 GWR produces location-specific coefficient estimates, offering a more nuanced
442 understanding of spatially varying associations between LST and its predictors (Fotheringham
443 et al., 2009). The GWR model is formally expressed as:

444
$$y_i = \beta_0(u_i, v_i) + \sum_{k=1}^m (\beta_k(u_i, v_i) x_{ik}) + \varepsilon_i \quad (6)$$

445 where (ui, vi) are the coordinates of observation i, $\beta_k(u_i, v_i)$ are spatially varying coefficients,
446 xik are predictor variables, and ε_i denotes random error. In GWR, local parameters are
447 estimated using weighted least squares, where each observation is assigned a weight based
448 on its spatial proximity to the location being evaluated. These weights are determined by a
449 spatial kernel function and a bandwidth parameter that defines the extent of spatial
450 influence. Selecting an optimal bandwidth is therefore essential to balance the trade-off
451 between model bias and variance. In this study, the optimal bandwidth was identified through
452 an iterative optimization procedure that minimizes the corrected Akaike Information
453 Criterion (AICc) (Fotheringham et al., 2009). This approach ensures robust estimation of local
454 relationships while effectively accounting for spatial non-stationarity in the dataset. Such a
455 framework is particularly valuable in fire-affected landscapes, where the impacts of fire
456 intensity, aerosol loading, and surface characteristics on LST are inherently heterogeneous
457 and vary substantially across space.

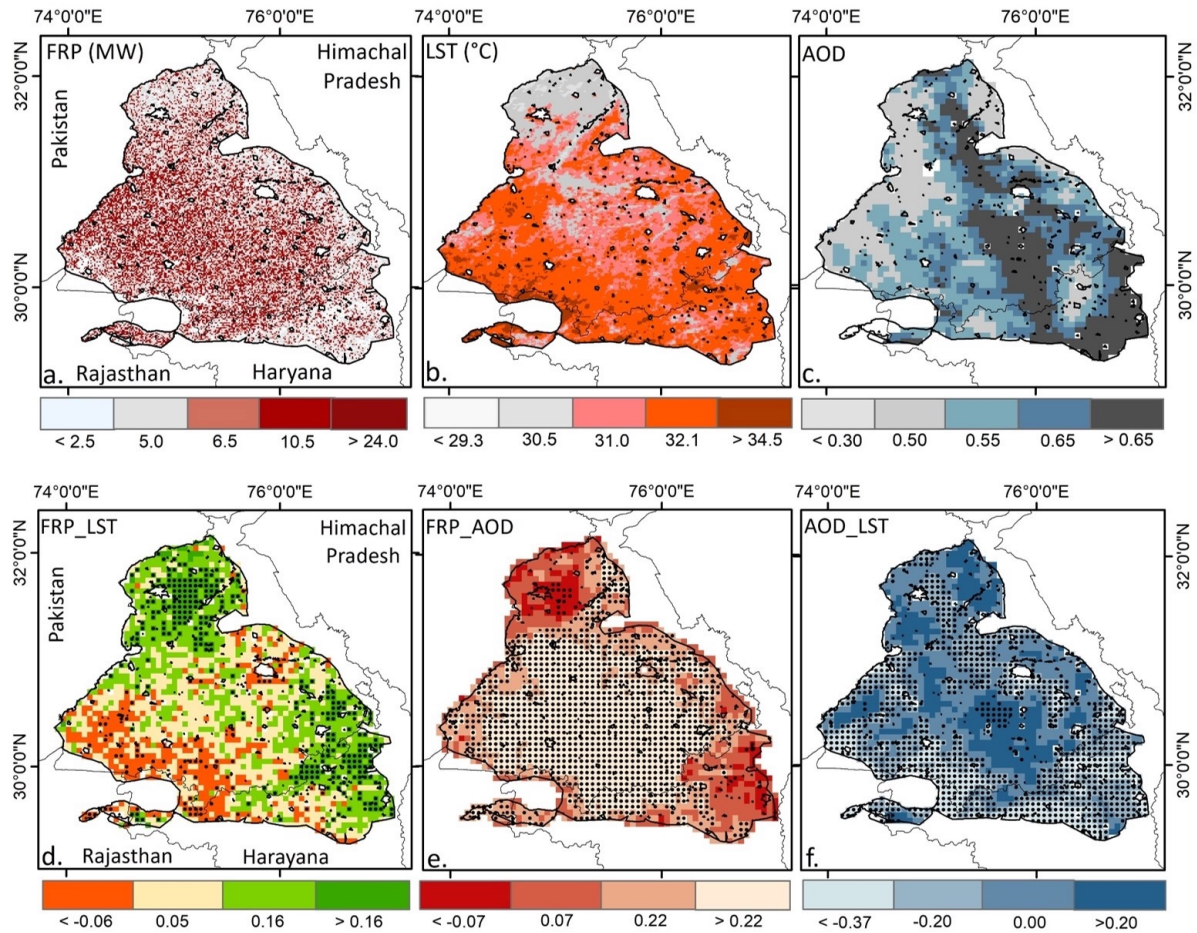
458

459

460 **3. Results and discussions**

461 **3.1 Spatial association between fire, aerosols and LST**

462 Spatial variations in FRP, LST and AOD averaged for October to November between
463 2017 and 2021 over extended geographical region is shown in Figure 4(a-c). While residue-
464 based FRP did not exhibit a distinct spatial pattern, temporal variations were prominent, with
465 monthly mean FRP in November ($310,188 \text{ MW month}^{-1}$) showing nearly a 100% increase
466 compared to October ($152,616 \text{ MW month}^{-1}$; Table S5). In contrast, the spatial pattern of LST
467 exhibited considerable heterogeneity, with relatively higher temperature observed in the
468 southern parts of the region that gradually declined northward. This north–south gradient
469 may be partially attributed to the proximity of the Himalayan foothills, where the cooler
470 mountainous environment likely offsets fire-induced surface warming. A gradual decline in
471 spatially averaged monthly mean LST was also accounted in November ($29.0 \pm 2.4 \text{ }^{\circ}\text{C}$)
472 compared to October ($31.0 \pm 1.6 \text{ }^{\circ}\text{C}$). A spatially distinct pattern in columnar aerosol loading
473 was evident across the extended geographical region, with elevated AOD (> 0.65) retrieved
474 over the central areas that gradually decreased towards its periphery (< 0.30). Such spatial
475 variability in aerosol loading is likely driven by differences in the intensity of residue-based
476 fires and the associated emissions of aerosols and trace gas precursors. Moreover, the
477 pronounced increase in monthly mean AOD (October: 0.59 ± 0.08 ; November: 0.82 ± 0.12)
478 likely reflects the intensification of fire during early November, compounded by concurrent
479 meteorological influences, most notably the seasonal decline in boundary layer height
480 (Banerjee et al., 2022).



481

482 Fig. 4. Spatial variations of FRP, LST and AOD over extended geographical region, 5-year mean
 483 FRP (a), LST (b) and AOD (c), and spatial correlation between FRP_LST (d), FRP_AOD (e)
 484 and AOD_LST (f). To compute spatial correlation, daily retrievals of FRP, AOD and LST
 485 were converted to a common 6x6 km² grid. Spatial correlation was computed for the
 486 entire duration and significant correlation ($P < 0.05$) is shown with black dot.

487

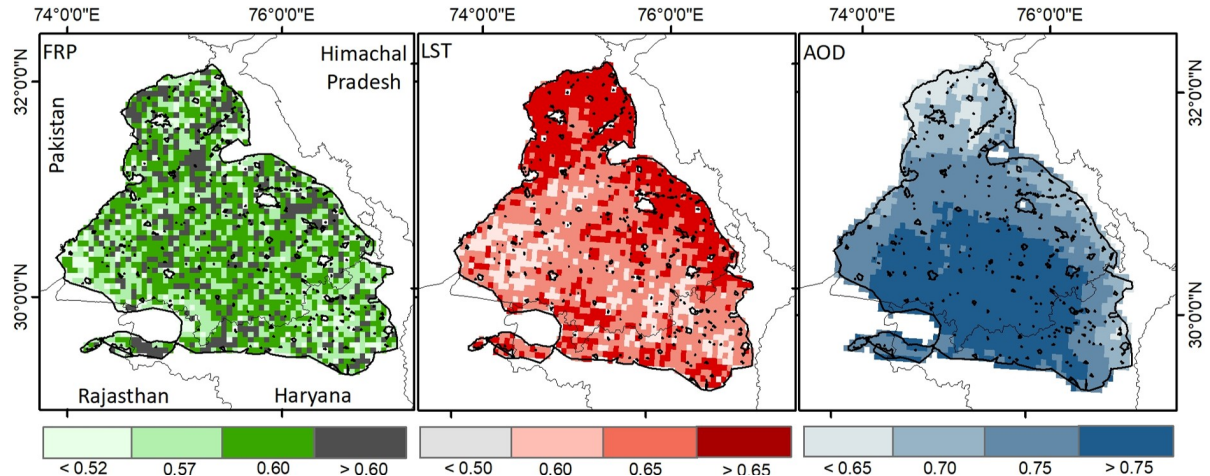
488 Spatial associations among VIIRS-derived FRP, MODIS LST, and VIIRS-based AOD daily
 489 retrievals were assessed over the extended geographical region (Fig. 4d-f). Spatial correlation
 490 between pixel-based FRP against LST reveals positive but spatially heterogeneous association
 491 across most parts of the study area, except in the southern region. A statistically significant
 492 relationship ($P < 0.05$) between FRP and LST underscores the potential influence of crop
 493 residue burning on surface temperature. Similarly, a significant association between FRP and
 494 AOD was observed across the central region, where fire intensity was notably higher than in
 495 surrounding areas. This spatial covariation between fire intensity and columnar aerosol
 496 loading further reinforces the influence of biomass-burning-induced emissions of aerosols

497 and their precursors on atmospheric aerosol abundance. Biomass-burning aerosols,
498 predominantly composed of carbonaceous soot particles, are known to modulate the thermal
499 budget of the lower atmosphere (Freychet et al., 2019; Xu et al., 2021). The spatial association
500 between AOD and LST further supports the existence of a fire–aerosol–surface temperature
501 nexus over northwestern India. A comparatively weak yet statistically significant positive
502 correlation between AOD and LST likely reflects lower-atmospheric warming induced by
503 smoke aerosols, consistent with the similar warming effect over western United States during
504 2017 California wildfire (Gomez et al., 2024).

505 **3.2 Evaluation of Hurst exponent**

506 The Hurst exponent was evaluated to assess the long-term persistence of fire
507 intensity, surface temperature, and aerosol loading time series over the extended
508 geographical region. In principle, the Hurst exponent is used to quantitatively distinguish a
509 purely stochastic time series ($H = 0.50$) from a persistent ($H > 0.50$) or anti-persistent ($H <$
510 0.50) time series of pixel-based FRP, LST, and AOD, following the methodology described in
511 Markonis and Koutsoyiannis (2016) and Chen et al. (2022).

512 As shown in Figure 5, nearly the entire extended geographical region of northwestern
513 India exhibits Hurst exponent values greater than 0.50 for FRP, with relatively higher values
514 (0.60–0.70) concentrated toward its central zone. Although variations in Hurst exponent for
515 FRP was spatially inconsistent, primarily due to temporal and spatial fluctuations in fire
516 intensity, the FRP time series over most of the region indicates statistical persistence.
517 Similarly, elevated Hurst exponent values for LST (>0.50) across the region also exhibits
518 persistence at long run. Notably, the northern portion of the study region shows slightly
519 higher Hurst exponent values compared to the southern part. For regional aerosol loading,
520 except few isolated patches, comparatively high Hurst exponent values (>0.75) were
521 observed over the central region. Notably, this area also coincides with zones characterized
522 by high AOD (>0.65) and a statistically significant FRP–AOD association. Overall, the Hurst
523 exponent analysis indicates that the observed FRP, LST, and AOD time series across most of
524 the residue-burning region exhibit statistical persistence.



527 Fig. 5. Estimating FRP (MW), LST ($^{\circ}\text{C}$) and AOD time-series persistence in extended
528 geographical region.

529 However, interpretation of the Hurst exponent results should be approached with
530 caution. The five-year dataset used here may not be sufficient to derive statistically robust
531 estimates. For the same reason, trend analysis was not undertaken, as the limited dataset
532 constrains the reliability of such estimates and falls beyond the scope of the present study.
533 Nonetheless, several studies have documented long-term trends in fire dynamics and aerosol
534 loading over northwestern India (e.g., Vadrevu and Lasko, 2018; Jethva et al., 2019; Singh et
535 al., 2020).

536 **3.3 Surface temperature and aerosols response to fire intensity**

537 Fire intensity in terms of pixel-based FRP, aerosol loading and surface temperature
538 were retrieved to compute corresponding daily and spatial means based on five years of
539 satellite retrievals. It is noteworthy that to account immediate response of fire intensity and
540 aerosol loading on surface temperature, all variables were retrieved exclusively over year-
541 specific intensive fire zones, having cumulative $\text{FRP} \geq 5 \text{ MW grid}^{-1}$, as illustrated in Fig. 2(b-f).

542 A distinct temporal pattern is evident in the FRP time series (Fig. 6a), which corresponds
543 closely with daily variations in fire counts (Fig. S4). Over northwestern India, FRP starts to
544 build-up typically in mid-October, peaks consistently during the first week of November, and
545 declines thereafter by mid-November. In contrast, the temporal pattern of the five-year mean
546 LST time series appears less pronounced, as daily retrievals exhibit substantial variability.
547 Regional LST demonstrates both interannual and intra-annual fluctuations, as illustrated in
548 Fig. S5. Notably, the FRP time series aligns well with the mean columnar aerosol loading,

underscoring the potential influence of aerosol and precursor emissions from widespread biomass burning. The characteristic rise in AOD during the first two weeks of November likely represents a direct response to intensified fire activity, as columnar AOD values consistently exceed 1.00 over the intensive fire zone. Interestingly, between October 25 and November 20 each year, approximately 90% of daily AOD observations surpass the five-year mean (0.74 ± 0.28), coinciding with an 800% increase in average FRP ($13,085 \pm 6,825$ MW) compared to the remainder of the season ($1,148 \pm 1,478$ MW). During this interval, the five-year mean columnar AOD exhibits a strong association with the aggregate FRP ($r = 0.46$) and mean LST ($r = 0.41$), whereas these associations weaken considerably outside this period (AOD-FRP: $r = 0.18$; AOD-LST: $r = -0.02$).

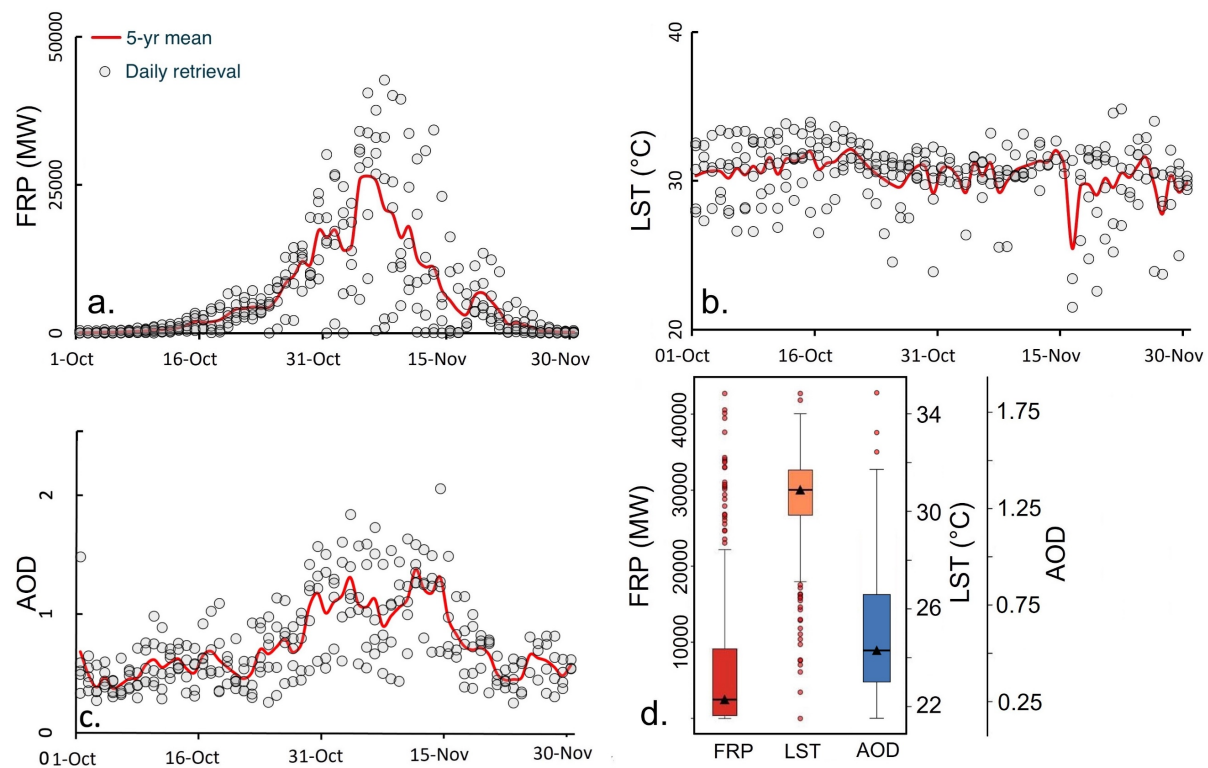


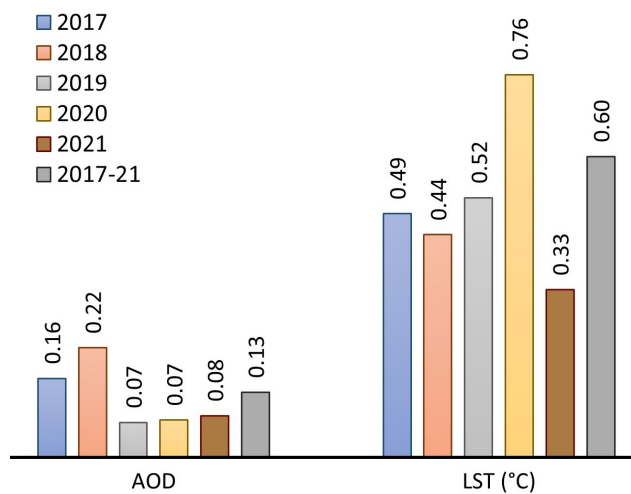
Fig. 6. Time series of five-year mean fire radiative power (FRP, a), land surface temperature (LST, b) and aerosol optical depth (AOD, c) against daily retrievals, (d) covariation of FRP, AOD and LST over intensive fire zone. Gray dots show daily retrievals from October to November (2017–2021), with the red line depicting the corresponding 5-year mean.

The temporal associations among FRP, AOD, and LST clearly demonstrate the immediate response of fire-induced variations in aerosol loading and surface temperature over northwestern India. Accordingly, in the subsequent section, these relationships were

567 modelled using a geospatial tree-based regression framework that integrates concurrent
568 temporal features (e.g., day-specific retrievals) and spatial predictors (e.g., regional
569 meteorology, aerosol loading, and fire intensity) to quantify and characterize the FRP–AOD–
570 LST nexus within the intensive fire zone.

571 **3.4 Fire induced change in LST and AOD**

572 The effect of crop residue burning on land surface temperature and aerosol loading
573 was assessed using a space-for-time approach by overlaying grid-based VIIRS LST, FRP, and
574 AOD datasets over the northwestern region experiencing recurrent fire. To remove potential
575 confounding effect, fire and no-fire grids were retained for comparison only when they
576 matched in terms of topography, meteorology, physical environment, vegetation and soil
577 characteristics, climatological mean LST and AOD, and surface property. Comparisons were
578 performed within defined strata containing grids with identical characteristics to ensure that
579 the quantified changes in LST and AOD could be attributed solely to fire. A total of 7489 paired
580 no-fire and fire grids were used between 2017 and 2021 to quantify the relative change in LST
581 and AOD. It is noteworthy that all grids, whether exhibiting fire or not, were selected from
582 within the extended geographical region to capture localized variations in temperature and
583 aerosol loading.



584
585 Fig. 7. Crop residue-based fire induced changes in land surface temperature and aerosol
586 loading.

587 As illustrated in Fig. 7, a consistent yet temporally dynamic increase in both LST and
588 AOD was observed over regions affected by residue-based burning compared with no-fire
589 zone. However, the magnitude of LST and AOD change across the fire zone was spatially

590 heterogeneous. On average, residue-based burning induced an increase of 0.60 °C in LST
591 during 2017–2021, with interannual variability ranging from 0.33 °C to 0.76 °C. This indicates
592 that residue burning exerts a persistent warming influence on land surface temperature, likely
593 driven by reduced evapotranspiration, enhanced shortwave absorption, increased sensible
594 heat flux, and fire-induced changes in surface albedo. However, a strong spatial heterogeneity
595 in LST and AOD modulation further indicates the potential influence of key confounding
596 factors and intensity of fire in regulating the change. The results of this study align with Liu et
597 al. (2019), who attributed a 0.15 °C rise in surface temperature over burned areas globally to
598 satellite-observed forest fires, as well as Liu et al. (2018), who documented a net warming
599 effect over the Siberian boreal forest. Additional evidence from Alkama and Cescatti (2016)
600 and Zhao et al. (2024) also indicates a positive linkage between forest fire occurrence, fire
601 intensity, and surface temperature. In contrast, the biophysical effects of agricultural residue
602 burning on land surface temperature remain poorly constrained. Zhang et al. (2020) reported
603 LST increases of 1–3 °C over three provinces in China associated with crop residue burning.
604 However, the feedback effects of meteorological covariates and systematic land-cover
605 differences on fire occurrence were not accounted for, leading to causal attribution of fire to
606 LST remains tentative.

607 A consistent annual increase in aerosol loading was also observed over the fire-
608 affected grids over northwestern India. A clear upward trend in AOD was noted across the
609 fire zones, with a mean increase of 0.13 AOD year⁻¹ and a range of 0.07–0.22 AOD year⁻¹. The
610 change in columnar aerosol loading, however, was spatially heterogeneous. Overall, the
611 increase in AOD from fire-associated emissions of aerosols and their gaseous precursors
612 reinforces the source-specific contribution of crop residue burning, a phenomenon well
613 documented in previous studies (Vinjamuri et al., 2020; Mhawish et al., 2022).

614 To quantify uncertainty in the estimated differences between fire-affected and non-
615 fire-affected grid cells, we further computed 95% confidence intervals for Δ LST and Δ AOD
616 using nonparametric bootstrapping. For each variable, 10,000 bootstrap samples were
617 generated by resampling grid cells with replacement, and the mean difference was
618 recalculated for each bootstrap replicate. The 2.5th and 97.5th percentiles of the resulting
619 sampling distribution were taken as the bounds of the 95% confidence interval (CI).
620 Nonparametric bootstrapping results into significant increase in both Δ LST (0.57°C; 95% CI:

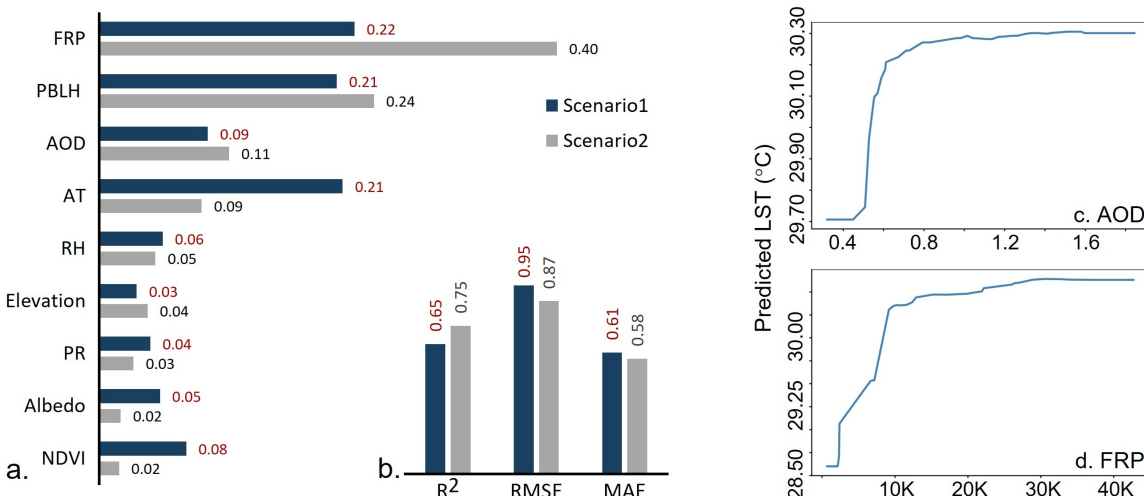
621 0.33–0.81°C) and Δ AOD (0.13; 95% CI: 0.08–0.17) in fire-affected regions. Because both CIs
622 do not overlap zero, these differences are statistically robust and unlikely to be due to
623 sampling variability.

624 **3.5 Spatial regression of fire intensity and aerosols on LST**

625 A machine learning algorithm was employed to establish the statistical association
626 between the dependent variable LST and multiple predictors including fire radiative power,
627 aerosol loading, regional meteorology (Fig. S6), surface properties, and vegetation
628 characteristics. All biophysical parameters, except SR and soil moisture, retrieved under two
629 pre-defined scenarios, (one) days with moderate-to-high fire intensity and (two) days with
630 sustained high fire intensity exhibiting a positive association with regional mean LST, were
631 used to model the FRP–AOD–LST relation. Relative feature importance (RFI) of selected
632 predictors was first evaluated for the fire season, and the marginal effects of FRP and aerosols
633 on LST were subsequently quantified. Figure 8(a) presents the normalized RFI values for all
634 predictors under both scenarios, and the Random Forest hyperparameter tuning procedure
635 is summarized in Table S6. RFI quantifies the sensitivity of regional LST to each predictor and
636 reflects their partial contribution to surface temperature variability. Fire radiative power
637 emerged as the dominant predictor under both scenarios, indicating the strong influence of
638 fire-related energy release on regional radiative balance, likely through reduced
639 evapotranspiration and fire-induced changes in surface albedo (Liu et al., 2018, 2019).
640 Notably, the RFI was substantially higher during period of sustained high-intensity burning
641 (Scenario 2; RFI = 0.40) compared with days characterized by moderate-to-high fire activity
642 (Scenario 1; RFI = 0.22), highlighting the stronger thermal response associated with intensive
643 burning condition.

644 Next to FRP, PBLH exerted a significant influence on LST (RFI: 0.21–0.24), followed by
645 atmospheric temperature (RFI: 0.09–0.21). The strong effect of PBLH on LST can be explained
646 by restricted turbulent mixing during shallow boundary-layer conditions in post-monsoon
647 season. A relatively low PBLH (mean \pm SD: 71 \pm 29 m) over northwestern India reduces vertical
648 mixing and traps fire-induced heat and aerosols close to the surface (Vinjamuri et al., 2020).
649 This enhances shortwave absorption, suppresses evaporative cooling, and limits turbulent
650 heat dissipation, resulting in a stronger and more persistent increase in LST. Another notable
651 finding was the modification of LST due to enhanced columnar aerosol loading during fire

652 season. The RFI of AOD varies from 0.09 to 0.11, indicating its influence on regional radiative
 653 budget. Residue burning releases aerosols and their gaseous precursors, which can exert
 654 significant radiative impacts and drive rapid adjustments in both surface and atmospheric
 655 temperature (Freychet et al., 2019; Xu et al., 2021). Fire-generated aerosols influence the
 656 energy balance through scattering and absorption of radiation, alterations in cloud
 657 microphysics, and changes in surface albedo via deposition of carbonaceous particles.
 658 However, the magnitude and direction of these radiative effects remain uncertain at the
 659 global scale (Tian et al., 2022). The partial influence of all other parameters, including
 660 meteorological variables, land characteristics and elevation was less significant (RFI < 0.30).



661
 662 Fig. 8. Normalized relative feature importance of predictor variables on LST (a), cross-
 663 validated evaluation of random forest performance (b), and partial dependence plots
 664 of LST on AOD (c) and FRP (d). Here, K indicates x1000. The PDP plots are based on
 665 scenario 2. Both RMSE and MAE have unit °C.

666
 667 The predictive skill of the random forest model was assessed using temporal block
 668 cross-validation to minimize temporal autocorrelation and prevent data leakage. Under both
 669 scenarios model performance was found satisfactory with R² varying from 0.65-0.75, marked
 670 with relatively low RMSE (0.87-0.95 °C) and MAE (0.58-0.61 °C). A satisfactory model
 671 performance also ensures that residue burning provide a clear LST response and the RF model
 672 was able to resolve non-linear land-atmosphere interactions, irrespective of the selected
 673 scenarios. Relatively better performance was however, achieved in scenario 2 during the fire

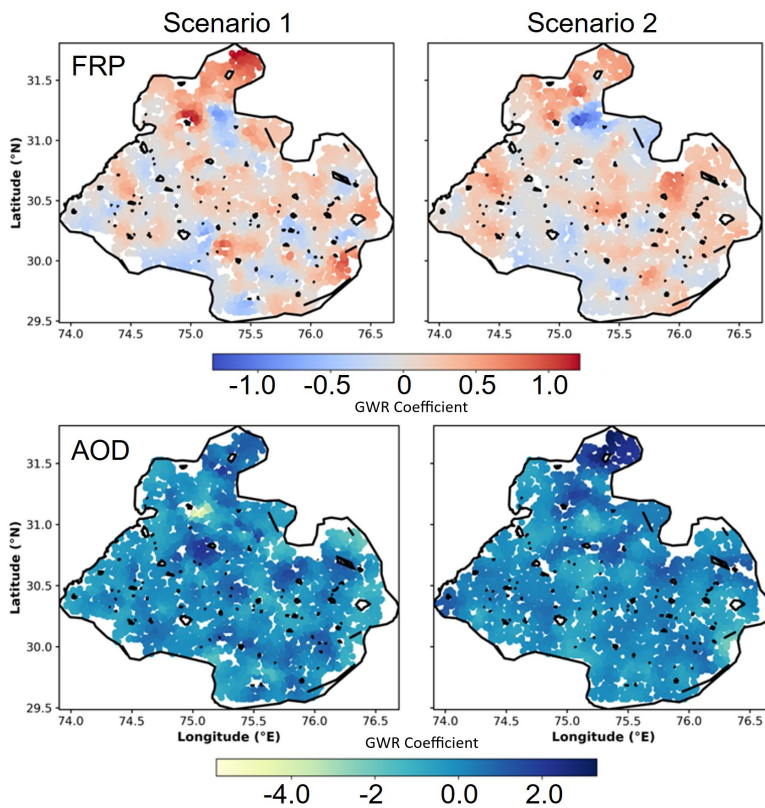
674 days having better spatial association between FRP and LST. Collectively, this confirms that
675 moderate-to-high intensity residue burning leaves a measurable and predictable thermal
676 signature on the land surface over northwestern India.

677 The partial dependence plots (PDPs) in Fig. 8(c–d) illustrate the marginal effects of FRP
678 and AOD on LST. These plots show the expected change in LST associated with variation in
679 each predictor while holding all other predictors constant. The estimated effects of both FRP
680 and AOD exhibit a non-linear, saturating response. LST increases sharply at low-to-moderate
681 values of each predictor but the effect progressively weakens at higher magnitudes,
682 approaching an asymptotic limit. This behaviour likely arises from the complex interplay of
683 radiative and thermodynamic processes associated with biomass-burning emissions. Fire-
684 originated aerosols exert both direct and indirect radiative effects whose magnitudes and
685 signs vary with aerosol loading and composition (Freychet et al., 2019; Xu et al., 2021; Tian et
686 al., 2022). At moderate aerosol loading, UV-absorbing black carbon aerosols may enhance
687 atmospheric heating and can transiently increase near-surface temperature (Jacobson, 2001).
688 Fire-induced convective plumes may initially enhance surface temperatures, whereas strong
689 aerosol build-up can reduce solar transmittance to the ground. Aerosol–cloud interactions
690 further contribute to non-linearity by modifying cloud microphysics, lifetime, and albedo,
691 altering the regional radiative balance. Additionally, aerosol-driven changes in boundary-layer
692 structure, evapotranspiration, and soil moisture introduce additional land–atmosphere
693 feedbacks. Together, these interacting processes operate across multiple spatial and
694 temporal scales and do not scale linearly with aerosol loading or fire intensity, producing the
695 observed non-linear LST response. The RF model therefore provides strong evidence that
696 both fire intensity and fire-derived aerosols exert measurable and non-linear effects on
697 regional LST, with potentially important implications for the regional radiative budget.

698 **3.6 Geographically weighted regression on LST**

699 A Global Moran's I test was first applied to assess spatial autocorrelation in LST across
700 the intensive fire zone for the cumulative five-year period. As shown in Table S6, Moran's I
701 was 0.225, accompanied by a high positive Z-score and a statistically significant p-value (<
702 0.001), indicating a clustered spatial pattern of LST that is highly unlikely (<1%) to have arisen
703 by random chance. Given this spatial dependence, GWR was employed to evaluate spatial
704 heterogeneity in the relationships between LST, FRP, and other predictors. All variables used

705 in the Random Forest model were incorporated into the GWR framework under both pre-
706 defined scenarios. Model specifications and performance metrics including bandwidth and
707 kernel details are mentioned in Table S8.



708
709 Fig. 9. Spatial distribution of FRP and AOD GWR coefficients across intensive fire zone.

710 GWR model demonstrated strong explanatory power, with global R^2 values exceeding
711 0.74, confirming that the selected predictors effectively captured spatial variability in LST. FRP
712 consistently showed a positive and spatially varying association with LST across both
713 scenarios, underscoring its dominant influence in fire-affected regions. Aerosol loading
714 demonstrated weak but spatially heterogeneous effects, reflecting localized differences in
715 aerosol–temperature interactions. Other predictors, including NDVI, RH, AT, PBLH, elevation,
716 and albedo (Fig. S7), exhibited local coefficients ranging from -0.76 to +0.23, indicating spatial
717 variability but comparatively weaker contributions to LST modulation across the study area.

718 Conclusions

719 The manuscript unfolds by identifying the geospatial variations in crop residue–based
720 fires and their associated impacts on aerosol loading and land surface temperature across
721 northwestern India. A brief methodology and key findings are summarized in Fig. S8. Based

722 on year-wise, pixel-level fire intensity, the geographical region with intensive fire activity was
723 initially delineated, and all satellite-derived and reanalysis datasets were subsequently
724 processed exclusively over the selected zone. A robust and consistent spatial correlation
725 between FRP, AOD, and LST was observed across multiple years, indicating potential fire-
726 induced perturbations in LST. The Hurst exponent analysis reaffirmed the long-term
727 persistence of fire intensity, surface temperature, and aerosol loading time series. A grid-
728 based analysis over the intensive fire zone revealed a significant increase in both LST and AOD
729 during the peak fire season.

730 The article further employs the Random Forest model and Geographically weighted
731 regression (GWR) to assess the potential influence of FRP and aerosol loading on LST, while
732 accounting meteorological covariates, physical environment, vegetation characteristic and
733 surface property as confounding factors within the selected zone. Two contrasting scenarios
734 were hypothesized to examine the FRP–LST–AOD nexus. Scenario 1 considered spatially
735 aggregated FRP from fire initiation to subsidence, whereas Scenario 2 focused on days
736 characterized by high-intensity fires exhibiting a strong positive correlation between FRP and
737 LST. In both the scenarios, the Random Forest regression successfully captured and mapped
738 FRP-induced modulation of LST, though with varying magnitudes. A distinct increase in FRP-
739 induced LST modulation was observed during high-intensity fire events. Both boundary layer
740 height and columnar aerosol loading also contributed partially, with aerosols' influence on
741 LST increasing during periods of intense release of fire energy. The Global Moran's I test
742 indicated significant spatial clustering of LST while GWR results further confirmed FRP and
743 AOD-modulated LST variations across northwestern India, highlighting strong spatial
744 heterogeneity in FRP-AOD-LST nexus.

745 This analysis reveals that the biophysical effects of crop residue-based fires across
746 northwestern India can substantially influence the regional radiative budget by altering LST.
747 The magnitude of LST modulation, however, depends on fire intensity and feedbacks from
748 regional meteorology. This study provides novel insights into residue-based fire induced
749 surface temperature dynamics in a region where recurrent fires have been historically linked
750 primarily with deteriorating air quality in Delhi and its surroundings. The observation-driven
751 analysis offers a comprehensive understanding of LST responses to residue burning and helps
752 reduce uncertainties in fire-induced modifications of the radiative budget. Nonetheless,

753 uncertainties remain due to unaccounted agricultural feedbacks, limited temporal coverage,
754 retrieval uncertainty in geospatial datasets, and the complexity in aerosol–meteorology
755 interactions. The multifaced influence of fire aerosols and energy on regional climate through
756 rapid atmospheric and land surface adjustments, remains complicated at the global level. Our
757 findings underscore the need for Earth system model–based simulations to better quantify
758 climate feedbacks from crop residue burning. Besides, assessing the underlying mechanisms
759 of fire-energy-induced changes in evapotranspiration, the radiative effects of aerosols, fire–
760 aerosol–meteorology feedbacks, and incorporating additional proxies could further reduce
761 the uncertainty in estimating radiative impacts from residue burning.

762

763 **Acknowledgments**

764 Authors acknowledges the fund received from Banaras Hindu University under Institute of
765 Eminence grant (6031). AP acknowledges fund received from Department of Science and
766 Technology under INSPIRE fellowship (IF220684). Authors also acknowledge open source
767 software like R (V4.4), Python (V3.7) and QGIS (V3.28) for extracting and plotting the dataset.

768 **Data Availability**

769 All the data used in this analysis are available freely. VIIRS and MODIS data can be accessed
770 via NASA Earthdata (<https://earthdata.nasa.gov>), and ERA5 reanalysis data is available from
771 ECMWF Copernicus (<https://cds.climate.copernicus.eu/>). SMAP Soil moisture data is available
772 at https://nsidc.org/data/spl1ctb_e. All dataset were last accessed on November 13, 2025.
773 We thank NASA for providing the VIIRS and MODIS data, and the Copernicus Climate Change
774 Service (C3S) for the ERA5 reanalysis data.

775 **Authors contributions**

776 AP: Data curation, formal analysis and interpretation; RS: Data curation, formal analysis; KA:
777 Data curation, formal analysis; NC: Data curation, formal analysis; TB: conceptualization,
778 methodology and interpretation, funding as well as writing and editing manuscript.

779 **Competing interests.** Authors declare that they have no conflict of interest.

780 **Supporting Information.** The supporting tables (8) and figures (8) are included in
781 supplementary file.

782

783 **References**

784 Aditi, K., Pandey, A., and Banerjee, T.: Forest fire emission estimates over South Asia using Suomi-NPP
785 VIIRS-based thermal anomalies and emission inventory, *Environ. Pollut.*, 366, 125441,
786 <https://doi.org/10.1016/j.envpol.2025.125441>, 2025.

787 Aditi, K., Singh, A., and Banerjee, T.: Retrieval uncertainty and consistency of Suomi-NPP VIIRS Deep
788 Blue and Dark Target aerosol products under diverse aerosol loading scenarios over South Asia,
789 *Environ. Pollut.*, 331, 121913, <https://doi.org/10.1016/j.envpol.2023.121913>, 2023.

790 Alkama, R., and Cescatti, A.: Biophysical climate impacts of recent changes in global forest cover,
791 *Science*, 351, 600–604, <https://doi.org/10.1126/science.aac8083>, 2016.

792 Andela, N., Morton, D. C., Giglio, L., Chen, Y., van der Werf, G. R., Kasibhatla, P. S., DeFries, R. S., Collatz,
793 G. J., Hantson, S., Kloster, S., Bachelet, D., Forrest, M., Lasslop, G., Li, F., Mangeon, S., Melton, J. R.,
794 Yue, C., and Randerson, J. T.: A human-driven decline in global burned area, *Science*, 356, 1356–1362,
795 <https://doi.org/10.1126/science.aal4108>, 2017.

796 Balwinder-Singh, McDonald, A. J., Srivastava, A. K., Jain, M., and Lobell, D. B.: Trade-offs between
797 groundwater conservation and air pollution from agricultural fires in northwest India, *Nat. Sustain.*, 2,
798 580–583, <https://doi.org/10.1038/s41893-019-0304-4>, 2019.

799 Banerjee, T., Anchule, A., Sorek-Hamer, M., and Latif, M. T.: Vertical stratification of aerosols over
800 South Asian cities, *Environ. Pollut.*, 309, 119776, <https://doi.org/10.1016/j.envpol.2022.119776>, 2022.

801 Banerjee, T., Shitole, A. S., Mhawish, A., Anand, A., Ranjan, R., Khan, M. F., Srithawirat, T., Latif, M. T.,
802 and Mall, R. K.: Aerosol climatology over South and Southeast Asia: Aerosol types, vertical profile, and
803 source fields, *J. Geophys. Res.-Atmos.*, 126, e2020JD033554, <https://doi.org/10.1029/2020JD033554>,
804 2021.

805 Bowman, D. M. J. S., Balch, J. K., Artaxo, P., Bond, W. J., Carlson, J. M., Cochrane, M. A., d'Antonio, C.
806 M., DeFries, R. S., Doyle, J. C., Harrison, S. P., Johnston, F. H., Keeley, J. E., Krawchuk, M. A., Kull, C. A.,
807 Marston, J. B., Moritz, M. A., Prentice, I. C., Roos, C. I., Scott, A. C., Swetnam, T. W., van der Werf, G.
808 R., and Pyne, S. J.: Fire in the Earth system, *Science*, 324, 481–484,
809 <https://doi.org/10.1126/science.1163886>, 2009.

810 Breiman, L.: Random forests, *Mach. Learn.*, 45, 5–32, <https://doi.org/10.1023/A:1010933404324>,
811 2001.

812 Brunsdon, C., Fotheringham, A. S., and Charlton, M. E.: Geographically weighted regression: A method
813 for exploring spatial nonstationarity, *Geogr. Anal.*, 28, 281–298, <https://doi.org/10.1111/j.1538-4632.1996.tb00936.x>, 1996.

815 Brunsdon, C., Fotheringham, S., and Charlton, M.: Geographically weighted regression, *J. Roy. Stat. Soc. Ser. D (The Statistician)*, 47, 431–443, <https://doi.org/10.1111/1467-9884.00145>, 1998.

817 Chen, J., Shao, Z., Huang, X., Zhuang, Q., Dang, C., Cai, B., Zheng, X., and Ding, Q.: Assessing the impact
818 of drought–land cover change on global vegetation greenness and productivity, *Sci. Total Environ.*,
819 852, 158499, <https://doi.org/10.1016/j.scitotenv.2022.158499>, 2022.

820 Chuvieco, E., Pettinari, M. L., Koutsias, N., Forkel, M., Hantson, S., and Turco, M.: Human and climate
821 drivers of global biomass burning variability, *Sci. Total Environ.*, 779, 146361,
822 <https://doi.org/10.1016/j.scitotenv.2021.146361>, 2021.

823 Copernicus Climate Change Service: Agrometeorological indicators from 1979 to present derived from
824 reanalysis, Copernicus Climate Change Service (C3S) Climate Data Store (CDS),
825 <https://doi.org/10.24381/cds.6c68c9bb>, accessed: 25 February 2025, 2020.

826 Daoud, J. I.: Multicollinearity and regression analysis, *J. Phys. Conf. Ser.*, 949, 012009,
827 <https://doi.org/10.1088/1742-6596/949/1/012009>, 2017.

828 Fotheringham, A. S., Brunsdon, C., and Charlton, M.: Geographically weighted regression, in: *The SAGE*
829 *Handbook of Spatial Analysis*, SAGE Publications, London, 243–254, 2009.

830 Freychet, N., Tett, S. F. B., Bollasina, M., Wang, K. C., & Hegerl, G.: The local aerosol emission effect on
831 surface shortwave radiation and temperatures. *Journal of Advances in Modeling Earth Systems*, 11,
832 806–817. <https://doi.org/10.1029/2018MS001530>, 2019.

833 Frazier, P. I.: A tutorial on Bayesian optimization. *arXiv preprint arXiv:1807.02811*, 2018.

834 Giglio, L., Descloitres, J., Justice, C. O., and Kaufman, Y. J.: An enhanced contextual fire detection
835 algorithm for MODIS, *Remote Sens. Environ.*, 87, 273–282, [https://doi.org/10.1016/S0034-4257\(03\)00184-6](https://doi.org/10.1016/S0034-4257(03)00184-6), 2003.

837 Gomez, J. L., Allen, R. J., and Li, K. F.: California wildfire smoke contributes to a positive atmospheric
838 temperature anomaly over the western United States, *Atmos. Chem. Phys.*, 24, 6937–6963,
839 <https://doi.org/10.5194/acp-24-6937-2024>, 2024.

840 Graham, M. H.: Confronting multicollinearity in ecological multiple regression, *Ecology*, 84, 2809–
841 2815, <https://doi.org/10.1890/02-3114>, 2003.

842 Granero, M. S., Segovia, J. T., and Pérez, J. G.: Some comments on Hurst exponent and the long
843 memory processes on capital markets, *Physica A*, 387, 5543–5551,
844 <https://doi.org/10.1016/j.physa.2008.05.064>, 2008.

845 Graham, M. H., Haynes, R. J., and Meyer, J. H.: Soil organic matter content and quality: Effects of
846 fertilizer applications, burning, and trash retention on a long-term sugarcane experiment in South
847 Africa, *Soil Biol. Biochem.*, 34, 93–102, [https://doi.org/10.1016/S0038-0717\(01\)00162-2](https://doi.org/10.1016/S0038-0717(01)00162-2), 2002.

848 Hurst, H. E.: Long term storage capacity of reservoirs, *Trans. Am. Soc. Civ. Eng.*, 6, 770–799, 1951.

849 Hsu, N. C., Herman, J. R., and Tsay, S. C.: Radiative impacts from biomass burning in the presence of
850 clouds during boreal spring in Southeast Asia, *Geophys. Res. Lett.*, 30, 1234,
851 <https://doi.org/10.1029/2002GL016485>, 2003.

852 Ichoku, C., Giglio, L., Wooster, M. J., and Remer, L. A.: Global characterization of biomass-burning
853 patterns using satellite measurements of fire radiative energy, *Remote Sens. Environ.*, 112, 2950–
854 2962, <https://doi.org/10.1016/j.rse.2008.02.009>, 2008.

855 Jacobson, M. Z.: Strong radiative heating due to the mixing state of black carbon in atmospheric
856 aerosols, *Nature*, 409, 695–697, <https://doi.org/10.1038/35055518>, 2001.

857 Jethva, H., Torres, O., Field, R. D., Lyapustin, A., Gautam, R., and Kayetha, V.: Connecting crop
858 productivity, residue fires, and air quality over northern India, *Sci. Rep.*, 9, 16594,
859 <https://doi.org/10.1038/s41598-019-52799-x>, 2019.

860 Kant, S., Sarangi, C., and Wilcox, E. M.: Aerosol processes perturb cloud trends over Bay of Bengal:
861 Observational evidence, *npj Clim. Atmos. Sci.*, 6, 132, <https://doi.org/10.1038/s41612-023-00442-5>,
862 2023.

863 Korontzi, S., McCarty, J., Loboda, T., Kumar, S., and Justice, C. O.: Global distribution of agricultural
864 fires in croplands from 3 years of Moderate Resolution Imaging Spectroradiometer (MODIS) data,
865 *Glob. Biogeochem. Cycles*, 20, GB2021, <https://doi.org/10.1029/2005GB002529>, 2006.

866 Lasko, K., and Vadrevu, K.: Improved rice residue burning emissions estimates: Accounting for
867 practice-specific emission factors in air pollution assessments of Vietnam, *Environ. Pollut.*, 236, 795–
868 806, <https://doi.org/10.1016/j.envpol.2018.01.114>, 2018.

869 Li, F., Zhang, X., Kondragunta, S., and Csiszar, I.: Comparison of fire radiative power estimates from
870 VIIRS and MODIS observations, *J. Geophys. Res.-Atmos.*, 123, 4545–4563,
871 <https://doi.org/10.1029/2017JD027823>, 2018.

872 Li, Z. L., Wu, H., Duan, S. B., Zhao, W., Ren, H., Liu, X., Leng, P., Tang, R., Ye, X., Zhu, J., and Sun, Y.:
873 Satellite remote sensing of global land surface temperature: Definition, methods, products, and
874 applications, *Rev. Geophys.*, 61, e2022RG000780, <https://doi.org/10.1029/2022RG000780>, 2023.

875 Liu, Z., Ballantyne, A. P., and Cooper, L. A.: Increases in land surface temperature in response to fire in
876 Siberian boreal forests and their attribution to biophysical processes, *Geophys. Res. Lett.*, 45, 6485–
877 6494, <https://doi.org/10.1029/2018GL078283>, 2018.

878 Liu, Z., Ballantyne, A. P., and Cooper, L. A.: Biophysical feedback of global forest fires on surface
879 temperature, *Nat. Commun.*, 10, 214, <https://doi.org/10.1038/s41467-018-08237-z>, 2019.

880 Logan, T. M., Zaitchik, B., Guikema, S., and Nisbet, A.: Night and day: The influence and relative
881 importance of urban characteristics on remotely sensed land surface temperature, *Remote Sens.*
882 *Environ.*, 247, 111861, <https://doi.org/10.1016/j.rse.2020.111861>, 2020.

883 Lan, R., Eastham, S. D., Liu, T., Norford, L. K., and Barrett, S. R. H.: Air quality impacts of crop residue
884 burning in India and mitigation alternatives, *Nat. Commun.*, 13, 6537,
885 <https://doi.org/10.1038/s41467-022-34284-6>, 2022.

886 Markonis, Y., and Koutsoyiannis, D.: Scale-dependence of persistence in precipitation records, *Nat.*
887 *Clim. Change*, 6, 399–401, <https://doi.org/10.1038/nclimate2894>, 2016.

888 Mhawish, A., Sarangi, C., Babu, P., Kumar, M., Bilal, M., and Qiu, Z.: Observational evidence of elevated
889 smoke layers during crop residue burning season over Delhi: Potential implications on associated
890 heterogeneous PM2.5 enhancements, *Remote Sens. Environ.*, 280, 113167,
891 <https://doi.org/10.1016/j.rse.2022.113167>, 2022.

892 NAAS (National Academy of Agricultural Sciences): Innovative viable solution to rice residue burning
893 in rice–wheat cropping system through concurrent use of Super Straw Management System-fitted
894 combines and Turbo Happy Seeder, National Academy of Agricultural Sciences, New Delhi, India, 2017.

895 Nguyen, H. M., and Wooster, M. J.: Advances in the estimation of high spatio-temporal resolution pan-
896 African top-down biomass burning emissions made using geostationary fire radiative power (FRP) and
897 MAIAC aerosol optical depth (AOD) data, *Remote Sens. Environ.*, 248, 111971,
898 <https://doi.org/10.1016/j.rse.2020.111971>, 2020.

899 Prasad, A. K., Singh, R. P., and Kafatos, M.: Influence of coal-based thermal power plants on aerosol
900 optical properties in the Indo-Gangetic Basin, *Geophys. Res. Lett.*, 33, L05805,
901 <https://doi.org/10.1029/2005GL023801>, 2006.

902 Puissant, A., Rougier, S., & Stumpf, A.: Object-oriented mapping of urban trees using Random
903 Forest classifiers. *Int. J. Appl. Earth Obs. Geoinf.*, 26, 235–245.
904 <https://doi.org/10.1016/j.jag.2013.07.002>, 2014.

905 Ramanathan, V., and Carmichael, G.: Global and regional climate changes due to black carbon, *Nat.*
906 *Geosci.*, 1, 221–227, <https://doi.org/10.1038/ngeo156>, 2008.

907 Ramana, M. V., Ramanathan, V., Podgorny, I. A., Pradhan, B. B., and Shrestha, B.: The direct
908 observations of large aerosol radiative forcing due to black carbon in the Himalayan region, *Geophys.*
909 *Res. Lett.*, 31, L05111, <https://doi.org/10.1029/2003GL018824>, 2004.

910 Remer, L. A., Kaufman, Y. J., Tanré, D., Mattoe, S., Chu, D. A., Martins, J. V., Li, R. R., Ichoku, C., Levy,
911 R. C., Kleidman, R. G., Eck, T. F., Vermote, E., and Holben, B. N.: The MODIS aerosol algorithm,
912 products, and validation, *J. Atmos. Sci.*, 62, 947–973, <https://doi.org/10.1175/JAS3385.1>, 2005.

913 Sayer, A. M., Hsu, N. C., Bettenhausen, C., and Jeong, M. J.: Validation and uncertainty estimates for
914 MODIS Collection 6 “Deep Blue” aerosol data, *J. Geophys. Res.-Atmos.*, 118, 7864–7872,
915 <https://doi.org/10.1002/jgrd.50600>, 2013.

916 Schroeder, W., Oliva, P., Giglio, L., and Csiszar, I. A.: The new VIIRS 375 m active fire detection data
917 product: Algorithm description and initial assessment, *Remote Sens. Environ.*, 143, 85–96,
918 <https://doi.org/10.1016/j.rse.2013.12.008>, 2014.

919 Seinfeld, J. H., and Pandis, S. N.: *Atmospheric Chemistry and Physics: From Air Pollution to Climate
920 Change*, John Wiley & Sons, Hoboken, New Jersey, 2016.

921 Sharma, N., Kaskaoutis, D. G., Singh, R. P., and Singh, S.: Impact of two intense dust storms and
922 associated mixing with biomass burning aerosols over the Indo-Gangetic Basin, *Atmos. Environ.*, 138,
923 167–180, <https://doi.org/10.1016/j.atmosenv.2016.05.002>, 2016.

924 Shahriari, B., Swersky, K., Wang, Z., Adams, R. P., & De Freitas, N.: Taking the human out of the loop:
925 A review of Bayesian optimization. *Proceedings of the IEEE*, 104(1), 148–175, 2015.

926 Shikwambana, L., and Mhangara, P.: Characterization of biomass burning aerosol over southern Africa
927 using multiple satellite data, *Int. J. Remote Sens.*, 39, 4764–4780,
928 <https://doi.org/10.1080/01431161.2018.1448481>, 2018.

929 Shikwambana, L., and Mhangara, P.: Analysis of the impact of biomass burning on tropospheric NO₂
930 over southern Africa during 2018, *Environ. Pollut.*, 261, 114204,
931 <https://doi.org/10.1016/j.envpol.2020.114204>, 2020.

932 Shikwambana, L., and Kganyago, M.: The contribution of biomass burning to carbon monoxide
933 concentrations in southern Africa: A case study of 2019, *Atmosphere*, 12, 878,
934 <https://doi.org/10.3390/atmos12070878>, 2021.

935 Singh, R. P., and Kaskaoutis, D. G.: Crop residue burning: A threat to South Asian air quality, *Eos Trans.
936 AGU*, 95, 333–334, <https://doi.org/10.1002/2014EO370001>, 2014.

937 Song, C. H., and Carmichael, G. R.: A three-dimensional modeling investigation of the evolution
938 processes of dust and carbonaceous aerosols over East Asia, *J. Geophys. Res.-Atmos.*, 106, 18131–
939 18154, <https://doi.org/10.1029/2000JD900511>, 2001.

940 Snoek, J., Larochelle, H., and Adams, R.P.: Practical bayesian optimization of machine learning
941 algorithms. *Advances in neural information processing systems*, 25, 2012.

942 Srivastava, A. K., Singh, S., Pant, P., Dumka, U. C., and Holben, B. N.: Black carbon aerosols over Manora
943 Peak in the Indian Himalayan foothills: Implications for climate forcing, *Environ. Res. Lett.*, 7, 014002,
944 <https://doi.org/10.1088/1748-9326/7/1/014002>, 2012.

945 Stein, A. F., Draxler, R. R., Rolph, G. D., Stunder, B. J. B., Cohen, M. D., and Ngan, F.: NOAA’s HYSPLIT
946 atmospheric transport and dispersion modeling system, *Bull. Am. Meteorol. Soc.*, 96, 2059–2077,
947 <https://doi.org/10.1175/BAMS-D-14-00110.1>, 2015.

948 Tiwari, S., Singh, A. K., Singh, S., and Pervez, S.: Aerosol climatology over Varanasi using MODIS and
949 MISR satellite data, *Air Qual. Atmos. Health*, 8, 301–309, <https://doi.org/10.1007/s11869-014-0285-8>, 2015.

950 Tian, C., Yue, X., Zhu, J., Liao, H., Yang, Y., Lei, Y., Zhou, X., Zhou, H., Ma, Y., and Cao, Y.: Fire–climate
951 interactions through the aerosol radiative effect in a global chemistry–climate–vegetation model,
952 *Atmos. Chem. Phys.*, 22, 12353–12366, <https://doi.org/10.5194/acp-22-12353-2022>, 2022.

953 Vadrevu, K. P., Ellicott, E. A., Giglio, L., Badarinath, K. V. S., Vermote, E., Justice, C., and Lau, W. K. M.:
954 Vegetation fires in the Himalayan region – Aerosol load, black carbon emissions and climate forcing,
955 *Remote Sens. Environ.*, 123, 324–334, <https://doi.org/10.1016/j.rse.2012.03.021>, 2012.

957 van der Werf, G. R., Randerson, J. T., Giglio, L., van Leeuwen, T. T., Chen, Y., Rogers, B. M., Mu, M., van
958 Marle, M. J. E., Morton, D. C., Collatz, G. J., Yokelson, R. J., and Kasibhatla, P. S.: Global fire emissions
959 estimates during 1997–2016, *Earth Syst. Sci. Data*, 9, 697–720, <https://doi.org/10.5194/essd-9-697-2017>, 2017.

961 Vadrevu, K. P., Lasko, K., Giglio, L., and Justice, C.: Analysis of Southeast Asian pollution episode using
962 satellite remote sensing data, *Atmos. Environ.*, 125, 512–522,
963 <https://doi.org/10.1016/j.atmosenv.2015.11.032>, 2016.

964 Vinjamuri, K.S., Mhawish, A., Banerjee, T., Sorek-Hamer, M., Broday, D.M., Mall, R.K. and Latif, M.T.:
965 Vertical distribution of smoke aerosols over upper Indo-Gangetic Plain. *Environmental pollution*, 257,
966 p.113377, 2020.

967 Wang, J., Christopher, S. A., Nair, U. S., Reid, J. S., Prins, E. M., Szykman, J., and Hand, J. L.: Mesoscale
968 modeling of Central American smoke transport to the United States: 1. “Top-down” assessment of
969 emission strength and diurnal variation impacts, *J. Geophys. Res.-Atmos.*, 111, D05S17,
970 <https://doi.org/10.1029/2005JD006416>, 2006.

971 Xu, L., Zhu, Q., Riley, W. J., Chen, Y., Wang, H., Ma, P.-L., and Randerson, J. T.: The Influence of Fire
972 Aerosols on Surface Climate and Gross Primary Production in the Energy Exascale Earth System Model
973 (E3SM), *J. Climate*, 34, 7219–7238, <https://doi.org/10.1175/JCLI-D-21-0193.1>, 2021.

974 Yang, J., and Zhao, Y.: Impacts of forest fires on surface temperature and precipitation in boreal
975 regions: An observational analysis, *Environ. Res. Lett.*, 15, 124046, <https://doi.org/10.1088/1748-9326/abc123>, 2020.

977 Zhao, T., Li, J., and Zhang, W.: Long-term changes in land surface temperature associated with
978 agricultural burning in eastern China, *Remote Sens.*, 13, 1215, <https://doi.org/10.3390/rs13061215>,
979 2021.

980